

High-Density Spherical Nanocarbon Clusters for Eco-Friendly Pouch-Type Ionic Liquid Supercapacitors with High Volumetric Energy Density and Rate Performance --Manuscript Draft--

Manuscript Number:	EST-D-23-06752
Article Type:	Research Paper
Keywords:	Carbon cluster, Eco-friendly, Pouch cell, Ionic liquid, Supercapacitor, Volumetric energy
Corresponding Author:	Wenxian Li University of New South Wales Sydney, AUSTRALIA
First Author:	Wei Zhang
Order of Authors:	Wei Zhang
	Junjie Shi
	Richard Webster
	Wenxian Li
	sean Li
Abstract:	<p>Improvement of volumetric energy density of carbon-based supercapacitors depends on the high working voltage window and volumetric capacitance without sacrificing rate performance. Ionic liquids and high-density porous carbons become emerging electrolytes and electrode materials due to their high decomposition voltage and large volumetric ion-accessible surface area, respectively. However, the influence of ion diffusion pathway in porous carbon on the capacitance performance is a challenging topic due to the various microstructures. Here, we report tailor-made spherical nanocarbon clusters acting as the electrode material of pouch-type ionic liquid supercapacitors to optimize the ion transport behavior in carbon electrodes. The obtained morphologies, close arrangements, and high densities of nanocarbon clusters shorten the ion transport pathway and facilitate ion accessibility for better rate capability and volumetric energy density. By using non-volatile EMIMBF₄ ionic liquid as the green electrolyte, carboxymethyl cellulose combined with styrene-butadiene rubber as eco-friendly aqueous binders of electrodes, the outstanding specific areal capacitance of 0.091 F m⁻² and volumetric capacitance of 53 F cm⁻³ are achieved at 0.5 A g⁻¹ with outstanding volumetric energy densities of 22.73 and 12.79 Wh L⁻¹ obtained at 481.25 and 23020.85 W L⁻¹, respectively. Both volumetric energy density and rate performance are considerably better compared to commercial activated carbon (YP-50F) which requires complicated, toxic and corrosive traditional activation processes for producing capacitive carbons.</p>
Suggested Reviewers:	<p>Li Xu, Ph.D Professor, Jiangsu University xulichem@ujs.edu.cn Prof Xu is an expert in renewable energy.</p>
	<p>MD Shahriar Hossain, Ph.D Associate Professor, The University of Queensland md.hossain@uq.edu.au A/Prof Hossain is an expert in renewable energy materials.</p>
	<p>Ting Liao, Ph.D Professor, Queensland University of Technology t3.liao@qut.edu.au Prof Liao is an expert on theoretical analysis of renewable energy materials.</p>
	<p>Weizhai Bao Nanjing University of Information Science and Technology weizhai.bao@nuist.edu.cn Prof Bao is an expert in supercapacitors.</p>

High-Density Spherical Nanocarbon Clusters for Eco-Friendly Pouch-Type Ionic Liquid Supercapacitors with High Volumetric Energy Density and Rate Performance

Wei Zhang[†], Junjie Shi[†], Richard Webster[‡], Wenxian Li^{†*} and Sean Li^{†*}

[†] *School of Materials Science and Engineering, UNSW Materials and Manufacturing Futures Institute, The University of New South Wales, Kensington, New South Wales 2052, Australia.*

[‡] *Electron Microscopy Unit, Mark Wainwright Analytical Centre, University of New South Wales, Sydney, NSW 2052, Australia*

Email: wenxian.li1@unsw.edu.au, sean.li@unsw.edu.au

Keywords: Carbon cluster, Eco-friendly, Pouch cell, Ionic liquid, Supercapacitor, Volumetric energy.

Abstract

Improvement of volumetric energy density of carbon-based supercapacitors depends on the high working voltage window and volumetric capacitance without sacrificing rate performance. Ionic liquids and high-density porous carbons become emerging electrolytes and electrode materials due to their high decomposition voltage and large volumetric ion-accessible surface area, respectively. However, the influence of ion diffusion pathway in porous carbon on the capacitance performance is a challenging topic due to the various microstructures. Here, we report tailor-made spherical nanocarbon clusters acting as the electrode material of pouch-type ionic liquid supercapacitors to optimize the ion transport behavior in carbon electrodes. The obtained morphologies, close arrangements, and high densities of nanocarbon clusters shorten the ion transport pathway and facilitate ion accessibility for better rate capability and

volumetric energy density. By using non-volatile EMIMBF₄ ionic liquid as the green electrolyte, carboxymethyl cellulose combined with styrene-butadiene rubber as eco-friendly aqueous binders of electrodes, the outstanding specific areal capacitance of 0.091 F m⁻² and volumetric capacitance of 53 F cm⁻³ are achieved at 0.5 A g⁻¹ with outstanding volumetric energy densities of 22.73 and 12.79 Wh L⁻¹ obtained at 481.25 and 23020.85 W L⁻¹, respectively. Both volumetric energy density and rate performance are considerably better compared to commercial activated carbon (YP-50F) which requires complicated, toxic and corrosive traditional activation processes for producing capacitive carbons.

1. Introduction

Over the last decades, renewable energy technologies have been thought as a solution to climate change and energy crises [1-3]. As an advanced energy storage device, the carbon-based supercapacitor plays an important role in renewable energy due to its special merits in high rate capability, long cycle life (>100 000 cycles) and low maintenance [4-6]. However, the low volumetric energy density confines their applications in limited space and high-energy consuming fields. The volumetric energy density of the carbon-based supercapacitor mainly depends on not only the device design and fabrication but also the pore texture of activated carbons loaded on two electrodes and the decomposition voltage of the electrolyte [5, 7]. Further improvement of the areal capacitance of the traditional activated carbons has been impeded by their high pore tortuosity and poor pore connectivity, which restrict the ion-accessible surface area of the electrodes [8-10]. Hence, the assembled supercapacitors normally exhibit poor rate performance with severe capacitance fading, especially at high current densities [11-13]. Although increasing the pore size can solve this problem to a certain extent, it results in the reduction of volumetric capacitance because of the lower bulk density of porous carbons [14, 15]. The optimization of pore size and bulk density of the porous carbons is

extremely difficult since these two parameters are interdependent, altering one would influence the other. Therefore, new types of porous carbon exhibiting outstanding areal and volumetric capacitances with high rate capability are eagerly awaited for the next generation of commercial supercapacitors.

Porous carbon spheres have been recognized as a promising material for achieving high volumetric capacitance in supercapacitor applications not only because of their large SSA, low electrical resistance, excellent fluidity and dispersity but also because the unique spherical morphology can achieve space-efficient packing for supercapacitor electrodes [16, 17]. It was reported that a high packing density of 0.75 g cm^{-3} was achieved by constructing monodispersed, submicron and N-doped microporous carbon spheres into pomegranate-like carbon microspheres. The assembled supercapacitor exhibited a high volumetric capacitance of 254 F cm^{-3} at 1 A g^{-1} [18]. However, similar to activated carbon, most porous carbon spheres have low-density issues, which limits further improvement of the volumetric capacitance of carbon themselves. Some approaches such as introducing heteroatom doping [19-21], high-density and defects [22] have been recently investigated. By using a heteroatom-codoping approach from tailoring carbon precursors, the obtained N, P, and S-codoped hierarchically porous carbon spheres with a high density of 0.8 mg mL^{-1} exhibited a good volumetric capacitance of 219 F cm^{-3} at 0.5 A g^{-1} [19]. By using a defect-enriched graphene block from the ball-milling, the outstanding volumetric capacitance of 215 F cm^{-3} and specific areal capacitances of 3.95 F cm^{-2} were achieved at 1 A g^{-1} . This superior performance is associated with the high density of 0.917 g cm^{-3} and “self-doping” defects that contribute to the electrical double-layer capacitance [22].

Another efficient strategy to improve the volumetric energy density of carbon-based supercapacitors is configuring with an electrolyte with a high decomposition voltage (e.g., organic and ionic liquid electrolytes [23-25]) or adding redox additives [26, 27]. Ionic liquids

1 have been hailed as inherent and competitive electrolytes ever since their introduction to the
2 field of electrochemical research. This is because they possess the ability to address numerous
3 drawbacks associated with traditional aqueous and organic electrolytes, including limited
4 potential ranges, volatility, and flammability [28]. Based on their chemical structure, ionic
5 liquids can be categorized into aprotic ionic liquids, protic ionic liquids, and zwitterionic
6 liquids. Among these, aprotic ionic liquids are well-suited for use as electrolytes in
7 supercapacitors due to their wider potential windows and excellent electrochemical stabilities
8 [29]. By using using an aprotic EMIMBF₄ ionic liquid as electrolyte, the ultrasmall carbon
9 nanospheres displayed a high energy density of 48 Wh kg⁻¹ at 14 kW kg⁻¹ and high capacitance
10 retention of 87.1% over 10000 cycles at 10 A g⁻¹ with an operating voltage of 3 V in a
11 symmetrical cell [30]. Similarly, the symmetrical supercapacitor using urea phosphate-derived
12 graphene aerogel as electrode material exhibited 78.3% capacitance retention after 5500 cycles
13 at 1 A g⁻¹ with a higher voltage window of 3.8 V [31].

14 Herein, we report tailor-made spherical nanocarbon clusters synthesized from a controllable
15 ball-milling of pristine graphite without adding diluents to improve the rate capability and
16 volumetric energy density of pouch-type ionic liquid supercapacitors by optimizing the ion
17 diffusion in carbon electrodes. The optimized supercapacitor exhibits a remarkable specific
18 areal capacitance of 0.091 F m⁻² and volumetric capacitance of 53 F cm⁻³ at a current density
19 of 0.5 A g⁻¹. An outstanding volumetric energy density of 22.73 Wh L⁻¹ is achieved at a power
20 density of 481.25 W L⁻¹ and it remains 12.79 Wh L⁻¹ at an extremely high power density of
21 23020.85 W L⁻¹. Such a performance is superior compared with the commercial activated
22 carbons (YP-50F), which has a volumetric energy density of 16.43 Wh L⁻¹ at 351.07 W L⁻¹ and
23 only 0.33 Wh L⁻¹ at 11783.50 W L⁻¹. Fabrication of high-performance ionic liquid pouch-type
24 supercapacitors with the eco-friendly aqueous binder (i.e., carboxymethyl cellulose and
25 styrene-butadiene rubber) and the spherical nanocarbon clusters synthesized in this work

demonstrates that the as-developed process is feasible and sustainable for high throughput industrial production.

2. Experimental section

2.1. Material synthesis

The engineered nanocarbons were synthesized by planetary ball-milling the pristine graphite in an ambient condition without using any diluents. 10 g natural graphite powders with a purity of 99.9995% and size of 325 mesh (Alfa Aesar) were milled in tungsten carbide media (250 mL of jar, 54 balls with 10 mm diameter, 400 g of balls in total) with a rotatory speed of 200 rpm for 3 to 72 hrs. To avoid excessively accumulated heat, the powders were milled for 0.25 hr with an interval of 0.25 hr. The ball-milled graphite was named BM200-X, where X is the milling time in hours.

2.2. Material characterization

The morphologies and microstructure information of the ball-milled graphite were analyzed by scanning electron microscopy (SEM, Carl Zeiss AURIGA) and transmission electron microscopy (TEM, Philips CM200). N₂ adsorption-desorption isotherms were measured to examine the porous structure by Micrometrics TriStar 3030 after vacuum degassing at 200 °C for 6 hrs. The specific surface area (SSA) was calculated by the Brunauer-Emmett-Teller model and the pore size distribution was analyzed using Barrette-Joynere-Halenda (BJH) model. The true density of the ball-milled graphite (ρ_{carbon}) was measured by Micromeritics AccPyc II 1340 Gas Pycnometer in a helium atmosphere. The average particle size was calculated by volume moment mean D [4,3] with Mastersizer 3000 (Malvern). The thermogravimetry (TG) analysis was performed with STA/TG-MS 449 F1 Jupiter (NETZSCH) ranging from 30 to 1000 °C with a ramping rate of 10 °C min⁻¹ in the air atmosphere. The graphic lattice structure of the

1 ball-milled graphite was carried out by X-ray diffraction analysis (XRD, PANalytical
2 Empyrean-II). The vibrational modes of carbon molecules were analyzed by Raman
3 spectroscopy (Renishaw in Via 2) with a 532 nm laser. The element content and surface
4 functional groups were examined by X-ray photoelectron spectroscopy (XPS, ESCALAB
5 250Xi Thermo Scientific).
6
7
8
9
10

11 **2.3. Electrochemical measurements**

12
13 To investigate the capacitive performance of large-scale ionic liquid supercapacitors, pouch-
14 type supercapacitors were fabricated. The two identical carbon electrodes inside were made by
15 mixing the ball-milled graphite, super-P carbon black (Alfa Aesar), carboxymethyl cellulose
16 (WALOCCEL CRT 30000 PA, DUPONT) and styrene-butadiene rubber (BM-400B, ZEON) in
17 deionized water with the mass ratio of 80:12:3:5. Subsequently, the slurry was uniformly
18 coated on the etched aluminum foil (Hohsen) using doctor blade technique. After drying at the
19 temperature of 85 °C for 12 hrs, the carbon electrodes with the active area of $3 \times 5 \text{ cm}^2$ and
20 mass loading of $\sim 5 \text{ mg cm}^{-2}$ were obtained. A piece of cellulose separator (TF4030, NKK) was
21 sandwiched by two electrodes and the pouch-type supercapacitor cells were sealed along their
22 edges in an Al laminated film. These edge-sealed pouch cells were subsequently dried at 120
23 °C for 12 hrs, then transferred into the glove box for the injection of neat EMIMBF₄ ionic liquid
24 electrolyte followed by the final sealing to finish the fabrication of the pouch cells.
25
26
27
28
29
30
31
32
33
34
35
36
37
38
39
40
41
42
43
44
45

46 The capacitive performance and cycle stabilities of the pouch cells were examined by Biologic
47 BCS-810. The voltage windows were set to 3.5 V. The cyclic voltammetry (CV) measurement
48 was performed at scan rates from 10 to 200 mV s⁻¹. The galvanostatic charge-discharge (GCD)
49 measurement was performed at current densities from 0.5 to 20 A g⁻¹. The electrochemical
50 impedance spectroscopy (EIS) was measured by Biologic BCS-810 with setting an AC
51 amplitude of 5 mV circuit voltage and frequencies ranging from 10 kHz to 10 mHz.
52
53
54
55
56
57
58
59
60
61
62
63
64
65

The specific capacitance (C_g , F g⁻¹), specific areal capacitance (C_A , F m⁻²) and volumetric capacitance (C_V , F cm⁻³) of one electrode in the pouch cell was calculated by the following equations, respectively:

$$C_g = \frac{4I}{2m \times \frac{\Delta V}{\Delta t}} \quad (1)$$

$$C_A = \frac{C_g}{S_{BET}} \quad (2)$$

$$C_V = C_g \times \rho_{particle} \quad (3)$$

Where I (A) is the discharge current, ΔV (V) is the voltage window excluding the IR drop at the beginning of the discharge curve, Δt (s) is the discharge time corresponding to ΔV , m (g) is the mass of the active material on a single electrode, SSA (m² g⁻¹) is the BET specific surface area and $\rho_{particle}$ (g cm⁻³) is the bulk density of the ball-milled graphite as shown in **Table 1**.

The gravimetric energy density (E_g , Wh kg⁻¹) and power density (P_g , W kg⁻¹), volumetric energy density (E_V , Wh L⁻¹) and power density (P_V , W L⁻¹) of the pouch cell were calculated by the following equations, respectively:

$$E_{g-cell} = \frac{\frac{1}{2} \times C_g \times \Delta V^2}{4 \times 3.6} \quad (4)$$

$$P_{g-cell} = \frac{3600 \times E_{g-cell}}{\Delta t} \quad (5)$$

$$E_{V-cell} = E_{g-cell} \times \rho_{particle} \quad (6)$$

$$P_{V-cell} = P_{g-cell} \times \rho_{particle} \quad (7)$$

Where ΔV (V) is the voltage window excluding the IR drop at the beginning of the discharge curve, Δt (s) is the discharge time corresponding to ΔV . Since our fabrication process of the pouch-type supercapacitor may be different from those published in the literature, the

volumetric energy and power densities in this work were calculated by the bulk density ($\rho_{particle}$) instead of device dimensions.

3. Results and discussion

3.1. Material characteristics

Fig. 1 schematically illustrates the principle of carbon structure modification from the pristine graphite to the clusters of nanocarbons engineered by planetary ball-milling technology. Without using diluents, the impact and shear stress pulverize crystalline graphite and introduce edge defects. Through prolonging the milling time, smaller graphite flakes, graphene-like sheets are formed, then gradually accumulated and rolled up as clusters of nanocarbons due to the high energy of abundant active edge defects. The SEM and TEM images in **Fig. 2** exhibit the milling duration dependence of the morphology in the same processing environment and **Fig. S1** shows the particle size distributions. As shown in **Fig. 2a**, the pristine graphite is ground into smaller graphite flakes (from $\sim 39.1 \mu\text{m}$ to $\sim 13 \mu\text{m}$ after 3 hrs). The appearance of graphene-like sheets shown in **Fig. 2b** suggests that the shear force from the high-energy ball-milling can exfoliate the graphene sheets from the graphite flakes. **Fig. 2c and d** show the graphite flakes are crushed and accumulated into fluffy clusters of nanocarbons with a few smaller graphene-like sheets after 9 hrs. For the longer milling duration of 54 hrs (**Fig. 2e to i**), the cluster size of nanocarbons is reduced to $\sim 6.6 \mu\text{m}$ and the surface of the cluster is smoothened. In addition, the cores of the clusters become less transparent to the electron beams of TEM due to their higher densities. As shown in **Fig. 2l**, by increasing the milling time up to 72 hrs, the cluster size is further reduced to $\sim 4.6 \mu\text{m}$ with less graphene-like structure appearing in the clusters. As a reference, the TEM images of the graphite milled with different rotational speeds of 100 and 300 rpm are shown in **Fig. S2** for comparison. Although we can achieve similar results in the morphology modification with different rotational speeds of the ball-

milling, the efficiency is significantly different. For example, BM100-90 has a similar morphology to BM200-9. While similar morphologies are observed for BM300-18 and BM200-72. However, lowering rotational speed results in larger and thinner graphene-like sheets whereas the higher rotational speed destroys the graphite crystalline structure quickly and results in a more compact and disordered carbon structure.

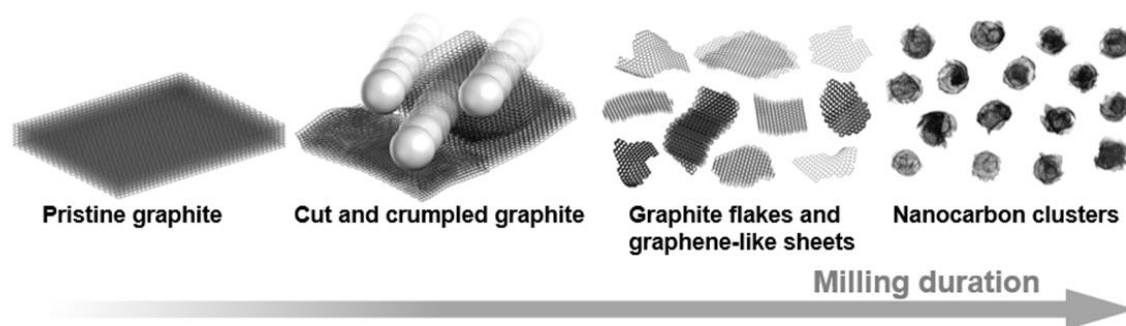


Fig. 1. Schematic illustration of ball-milling of pristine graphite.

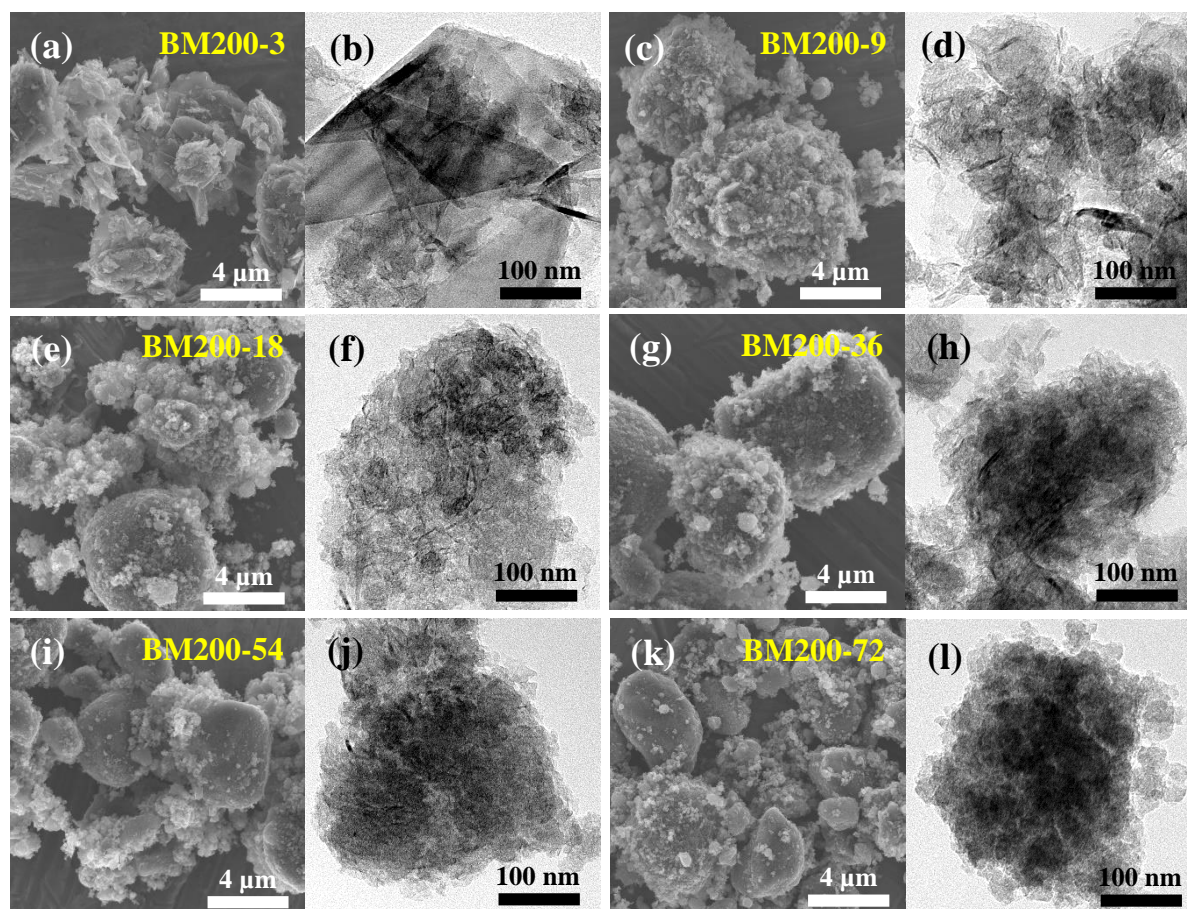


Fig. 2. (a, c, e, g, i and k) SEM images and (b, d, f, h, j and l) TEM images of carbon materials produced from ball-milling of graphite with a rotatory speed of 200 rpm for 3 to 72 hrs. (a, b) BM200-3, (c, d) BM200-9, (e, f) BM200-18, (g, h) BM200-36, (i, j) BM200-54 and (k, l) BM200-72.

Fig. 3a plots the N₂ adsorption-desorption isothermal curves of the pristine graphite and the ball-milled graphite measured at -196 °C. The pristine graphite shows a flat behavior, indicating its non-porous structure. Based on the classification method of International Union of Pure and Applied Chemistry (IUPAC) updated in 2015 [32], all the ball-milled graphite exhibit the mixed behaviors of type I (a) and IV (a) with an H₄-type hysteresis loop. By increasing the milling time, the N₂ adsorption isotherms of the ball-milled graphite at the very low relative pressure ($P/P_0 < 0.01$) show a rising tendency, demonstrating the increase of micropore volume. The graphite milled for 9 hrs (BM200-9) exhibits the highest micropore volume of 0.168 cm³ g⁻¹. It is interesting to note that the micropore volume of BM200-72 was reduced to 0.082 cm³ g⁻¹, indicating the micropore volume shrunk by the prolonged milling process. In general, the distinct hysteresis loops that appeared at moderate-high relative pressure ($0.45 < P/P_0 < 0.95$) are related to the mesoporous capillary condensation while the upward tendencies at the high relative pressure range ($0.95 < P/P_0 < 1$) are caused by the unsaturated macroporous capillary condensation in large pore size. The detailed pore structure parameters and SSA of these ball-milled graphite are summarized in **Table 1**. Among milled graphite, the mesopore volumes are firstly increased and then subsequently decreased, where the BM200-9 exhibits the maximum mesopore volume of 1.275 cm³ g⁻¹. **Fig. 3b** reveals the pore size distribution calculated using BJH model for each ball-milled graphite, demonstrating the milling time dependence of mesopore volume. For comparison, the inset shows the milling time dependence of SSA and the BM200-9 possesses the largest SSA of 1130 m² g⁻¹ due to its superior high porosity, which is also the largest SSA among the ball-milled graphite reported

in the literature (**Table. 2**). Either the shorter or longer milling time leads to a smaller SSA.

Hence, it is discernable that the pristine graphite is gradually exfoliated with abundant pores formed at the beginning of the milling process, and then both micropores and mesopores are collapsed and compressed into a compact structure by prolonging the milling process.

The XRD spectra of the pristine graphite and the ball-milled graphite are shown in **Fig. S3**. For the pristine graphite, the spectra show the strongest characteristic peak at 26.7° and other peaks at 42.5° , 44.7° , 54.8° and 77.6° (with a measurement error of 0.05°) correspond to the (002), (100), (101), (004) and (110) plane of crystalline graphite, respectively. Increasing the milling time, the relative intensity of (002) peak is weakened, broadened and downshifted to 25.2° , showing the longer milling time produces more disoriented and smaller carbons with some extent of lattice relaxation. Characteristic peaks other than carbon were not observed, demonstrating the contamination from the milling process is limited. The effects of milling time on the interlayer d-spacing and full width half maximum (FWHM) of (002) peak are shown in **Fig. 3c**. It can be seen that the d-spacing increases from the typical 0.334 nm of graphite to 0.353 nm of BM200-72. Except for the lattice relaxation, the higher extent of disordering and heteroatom doping (e.g., oxygen and nitrogen) from the prolonged milling process are thought to be responsible for the lattice expansion [33]. In addition, the FWHM of (002) peak increases from 0.26° to 6.96° , suggesting the smaller grain size and higher extent of crystallographic disordering are produced by prolonging the milling time. Due to the nature of carbon coherent bonds in graphite, we consider that the effects of size reduction on the FWHM are much stronger than the internal strain caused by crystallographic disordering. The apparent up-turned tail at the low angle scattering indicates the presence of high porosity in carbons [34]. The inset shows the XRD diffraction patterns in the range from 5° to 10° , indicating the porosity of the ball-milled graphite first increased to result in the fluffy morphologies, and then decreased to produce the compact structure by prolonging the milling time. This verifies the

1 results from the SEM, TEM and also the N₂ adsorption-desorption isotherm analysis above.
2 Moreover, the influence of milling parameters, such as filling ratio, ball to graphite mass ratio,
3 rotational speed and milling time on crystallographic structures and contamination of graphite
4 are shown in **Fig. S4**. We conclude that more compact and disordered nanocarbons are formed
5 by increasing the filling ratio, ball to graphite mass ratio, rotational speed or milling time.
6 Hence, choosing the appropriate milling parameters is important for producing high-
7 performance capacitive carbons (refer to Supplementary Information for a detailed discussion).
8

9
10 **Fig. S5** plots temperature-dependent weight loss of the pristine and the ball-milled graphite by
11 thermogravimetric (TG) analysis. It is demonstrated that the weight loss behaviors of the ball-
12 milled graphite are strongly related to the internal energy of the systems that are determined by
13 the grain size and the extent of crystallographic disordering in the materials [35]. The TG
14 parameter of T_{1/2}, which is the temperature at half of the total weight loss in the process of
15 graphene sheet burnout, is used to provide a qualitative reference for both the graphene sheet
16 dimensions and the defect density. The ΔT , referring to the temperature range of the burnout,
17 is related to the polydispersity of the graphene products [36]. As shown in **Fig. 3d**, the ΔT -T_{1/2}
18 thermal phase diagram (TPD) exhibits the morphological classification directly related to the
19 corresponding sizes and crystallinity of the ball-milled graphite in this work. It is found that
20 with increasing the milling time, the ball-milled graphite first turns into graphene-like sheets,
21 then the nanocarbons or activated carbons. Meanwhile, both the polydispersity and size of the
22 ball-milled graphite are decreased.
23

24
25 Raman spectra shown in **Fig. S6** reveal the specific vibration modes and graphitization degree
26 of the ball-milled graphite. The Raman spectra of D and G bands between 900 and 1900 cm⁻¹
27 were deconvoluted into five peaks located at ~1250 cm⁻¹ (Lorentzian), ~1340 cm⁻¹ (Lorentzian),
28 ~1485 cm⁻¹ (Gaussian), ~1575 cm⁻¹ (Lorentzian) and ~1610 cm⁻¹ (Lorentzian). They are related
29 to D₄, D₁, D₃, G and D₂ bands, respectively (**Fig. S7**) [37, 38]. The G band represents the in-
30

plane bond-stretching motion of sp^2 in ordered graphitic lattices while D1 and D2 bands are associated with disordered graphitic lattices [39, 40]. D3 band is attributed to the interstitial defects of distributed amorphous carbons [41] while D4 band governs the C-C and C=C stretching vibration modes of sp^2 - sp^3 bonds (e.g., heteroatom doping) [42]. The intensity ratios of D1/G and D1/D2 are widely used to determine the disordering degree of carbons and also the nature of defects in graphene [43, 44]. As shown in **Fig. 3e**, the I_{D1}/I_G ratio increases from 0.04 (pristine graphite) to 1.54 (BM200-72), indicating the significant disordering of carbon atomic arrangement. It is reported that the I_{D1}/I_{D2} ratio is ~ 13 for sp^3 -defects, ~ 7 for vacancies and ~ 3.5 for the edge defects in graphite [43]. In our work, the I_{D1}/I_{D2} ratio remains at a nearly constant value of ~ 3.0 for all ball-milled graphite, suggesting that edge defects are the dominants. The inset shows the 2D bands of the ball-milled graphite at $\sim 2700\text{ cm}^{-1}$. The decrease of intensity, broadening as well as downshifting of the 2D band with increasing the milling time indicates the occurrence of graphite delamination with the C-C bond breaking and the edge selective functionalizing (i.e. oxygen and nitrogen attached to the defect sites) [45].

The surface functional groups of the ball-milled graphite were verified by XPS as shown in **Fig. S8**. There are no other characteristic peaks of impurities that appeared in the XPS spectra except for carbon, oxygen and nitrogen. The oxygen and nitrogen functional groups on the surface of carbon materials play an important role in increasing the surface wettability of the liquid electrolyte on the carbon electrodes, which significantly enhances the ion diffusion within the electrodes and introduces an additional pseudocapacitance [46]. It has been widely reported that the milling process can dope oxygen [47] and nitrogen [48] into the graphite. Therefore, it is not surprising if the oxygen and nitrogen dopants appeared in the ball-milled graphite in the air atmosphere (79% N_2 and 21% O_2) although its XPS signal is very weak. In addition, the XPS C_{1s} can be deconvoluted into seven peaks at 284.5, 285.3, 286.3, 287.5, 288.7, 289.3 and 290.5 eV, which are corresponding to the characteristic spectra of sp^2 C, sp^3 C, C-

1 N, C-O, C=O, O=C-O and π - π^* satellite peaks, respectively [49]. As shown in **Fig. 3f**, the
2 oxygen content increases from 0.93 to 3.1 at.% and nitrogen content increases from 0 to 1.1
3 at.%, implying that the longer milling time results in the introduction of more oxygen and
4 nitrogen surface functional groups. Moreover, the peak-fitting of XPS spectra of O_{1s} and N_{1s}
5 for the ball-milled graphite (using BM200-36, BM200-54 and BM200-72 as examples) are
6 shown in **Fig. S9**, demonstrating the existence of C-O, C=O, pyridinic N and pyrrolic N in the
7 ball-milled graphite. The homogeneous doping of oxygen and nitrogen atom was further
8 verified from the elemental distribution mapped by electron dispersive spectroscopy (EDS) in
9 **Fig. 4**. Moreover, the XPS results also reveal that the sp²/sp³ ratio of the ball-milled graphite
10 decreases from 8.15 (BM200-3) to 5.89 (BM200-72), suggesting more sp³ defected carbon
11 formed along with the oxygen and nitrogen doping by increasing the milling time [50]. This
12 may be the mechanism underpinning the phenomenon of interlayer d-spacing increase
13 observed in the ball-milled graphite.
14
15
16
17
18
19
20
21
22
23
24
25
26
27
28
29
30
31
32
33
34
35
36
37
38
39
40
41
42
43
44
45
46
47
48
49
50
51
52
53
54
55
56
57
58
59
60
61
62
63
64
65

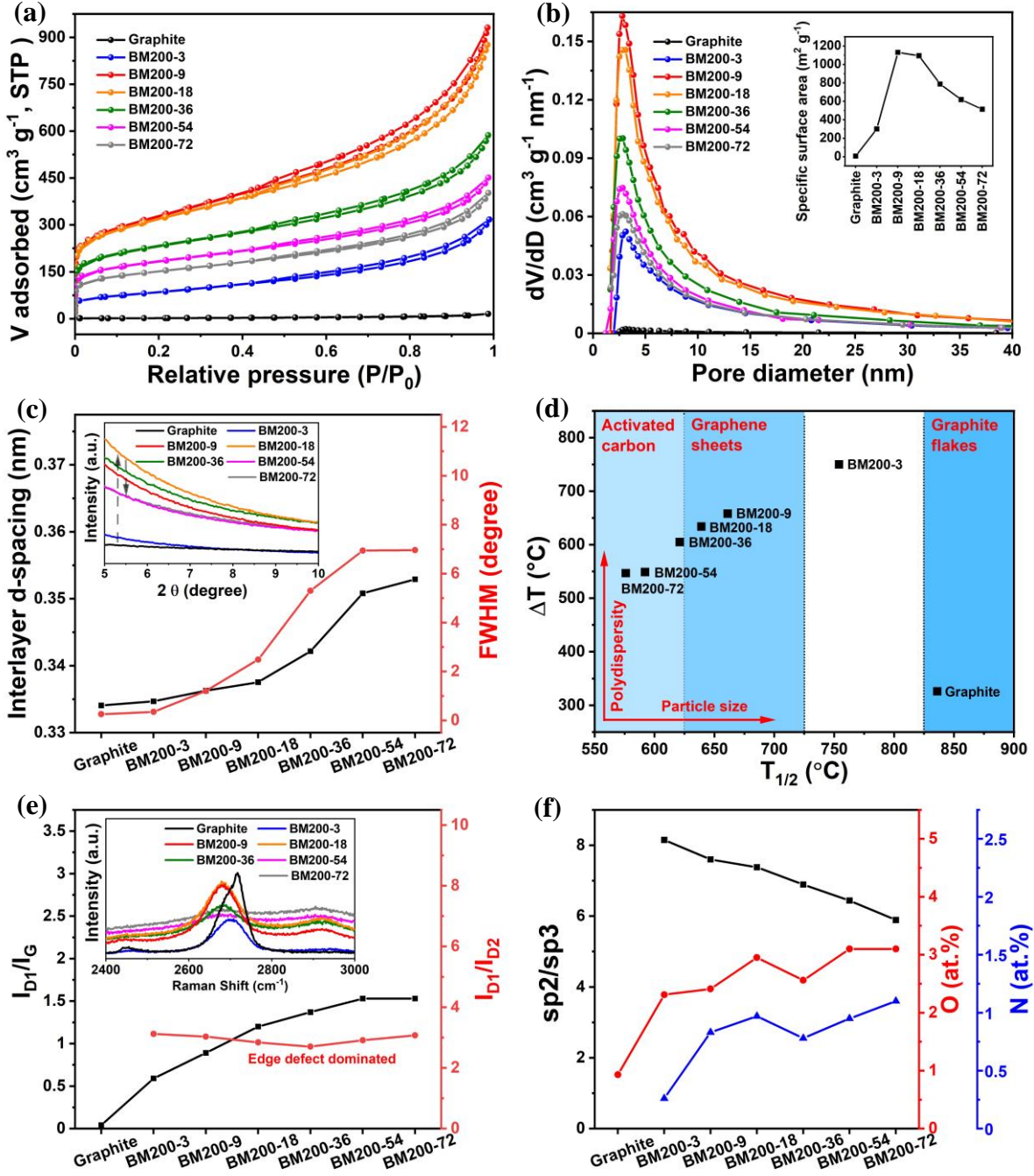


Fig. 3. The characterization of ball-milled graphite. (a) N₂ adsorption-desorption isotherms. (b) Pore size distribution based on the BJH model (the inset shows the SSA). (c) XRD parameters based on XRD patterns (the inset shows the low angle diffraction pattern). (d) TPD based on TG diagrams. (e) Raman parameters based on Raman spectra (the inset shows the 2D band). (f) XPS parameters based on XPS survey spectra.

Table 1. SSA, pore structure, XRD, Raman and XPS parameters of ball-milled graphite.

Sample	SSA ^[a] (m ² g ⁻¹)	V _{total} ^[b] (cm ³ g ⁻¹)	V _{micro} ^[c] (cm ³ g ⁻¹)	V _{meso} ^[d] (cm ³ g ⁻¹)	D _{av.pore} ^[e] (nm)	ρ _{particle} ^[f] (g cm ⁻³)	d-spacing (nm)	I _{D1} /I _G	I _{D1} /I _{D2}	sp ² /sp ³
Graphite	6	-	-	-	-	2.130	0.334	0.04	-	-
BM200-3	301	0.492	0.043	0.449	1.64	1.087	0.335	0.59	3.12	8.15
BM200-9	1130	1.443	0.168	1.275	5.11	0.547	0.336	0.89	3.03	7.60
BM200-18	1094	1.358	0.160	1.198	4.96	0.581	0.337	1.20	2.84	7.38
BM200-36	788	0.905	0.124	0.781	4.60	0.787	0.342	1.37	2.70	6.89
BM200-54	619	0.695	0.101	0.594	4.49	0.947	0.351	1.53	2.91	6.44
BM200-72	514	0.620	0.082	0.538	4.82	1.028	0.353	1.54	3.07	5.89

^[a] Specific surface area based on the BET method^[b] Total pore volume at P/P₀ = 0.99.^[c] Micropore volume calculated using the t-plot method.^[d] Mesopore volume = V_{total} - V_{micro}^[e] Average pore width = (4 × V_{total}) / SSA^[f] ρ_{particle} = 1 / (V_{total} + 1/ρ_{carbon})**Table 2.** Comparison of the SSA of BM200-9 with other ball-milled graphite reported in literature.

Material	Material of jar and balls	rpm for hrs	Filling	Post- purification	SSA (m ² g ⁻¹)	Reference
IGnP	Stainless steel	500 for 48	I ₂	Yes	772	[51]
GCM	Stainless steel	600 for 6	CaC ₂	Yes	597	[52]
10h-milled	Stainless steel	400 for 10	Ar	No	416	[53]
HGnP	Stainless steel	500 for 48	H ₂	Yes	437	[54]
HSG-20	Stainless steel	400 for 20	Air	-	580	[55]
HECG	Stainless steel	500 for 48	Air	Yes	631.8	[56]
EFGnPs	Stainless steel	750 for 48	Air	Yes	678.7	[57]
GO-24h	Stainless steel	340 for 24	Air	Yes	188.25	[45]
C-24h	Stainless steel	600 for 24	Air	-	666	[47]
F-24h	ZrO ₂	600 for 24	Air	-	730	

Z-H	ZrO ₂	400 for 80	H ₂	Yes	530	[58]
GNS	Ceramic	500 for 12	Sylitol	Yes	117	[59]
BM200-9	WC	200 for 9	Air	No	1130	This work

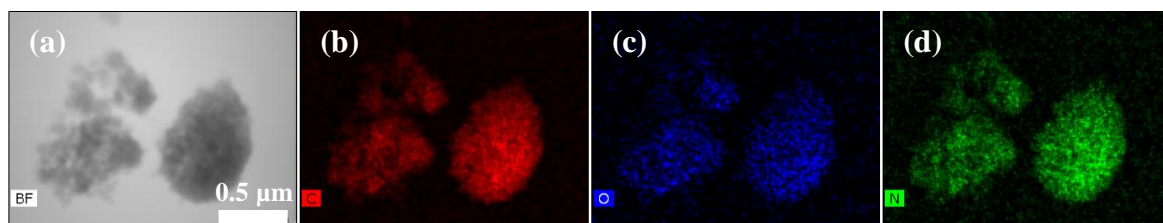


Fig. 4. (a) TEM image of BM200-36 and corresponding EDS elemental mapping of (b) carbon, (c) oxygen and (d) nitrogen.

3.2. Electrochemical properties in an aqueous binder-based pouch-type supercapacitor using neat EMIMBF₄ ionic liquid electrolyte.

To better understand the electrochemical performance of the pristine and the ball-milled graphite for practical applications, the symmetrical pouch-type supercapacitors were assembled using green aqueous carboxymethyl cellulose and styrene-butadiene rubber as the binder and neat EMIMBF₄ ionic liquid as the electrolyte. The CV curves of these pouch cells at a scan rate of 50 mV s⁻¹ are plotted in **Fig. 5a**. In contrast to the limited capacitance of the pristine graphite, the area coverage of CV curve for the ball-milled graphite increases with the increase of the milling time up to 18 hrs (BM200-18), then decreases for the prolonged milling time. All CV curves exhibit tilted quasi rectangular shapes with a voltage window up to 3.5 V, suggesting their good capacitive behaviors but with a bit high ESRs due to the high viscosity and low ionic conductivity of the ionic liquid. **Fig. 5b** shows GCD curves of the pouch cells measured at a current density of 0.5 A g⁻¹. The sharp IR drops can be seen at the top of the isosceles triangular GCD curves. With increasing the milling time, ESR calculated from the GCD curve firstly increases from 0.46 Ω (BM200-3) to 1.58 Ω (BM200-18), then slightly drops to 1.49 Ω (BM200-36), subsequently decreasing to 1.03 Ω (BM200-54) and 0.71 Ω (BM200-

72). This result is reasonable for the porous structure modified by the prolonged milling process, where the ion diffusion becomes unfavorable in shrinking mazy layered structures until the smaller clusters of nanocarbons are formed. Among these pouch cells, BM200-18 exhibits the longest charging-discharging time, implying that it has the highest specific capacitance over the others.

As shown in **Fig. 5c**, the ESRs determined by the X-axis intercept point at the lower frequency and the changing tendency of ESR is consistent with that of ESR calculated from GCD curves for the pouch cells. Moreover, nearly vertical curves at the low-frequency region appeared in all pouch cells indicating their good capacitive behaviors. The obtained R_{ct} obviously increases from 0.17 Ω (BM200-3) to 1.76 Ω (BN200-18) and then decreases to 0.49 Ω (BM200-72). Notably, the neat EMIMBF₄ electrolyte is an aprotic ionic liquid, which suppresses the redox reaction (i.e. pseudocapacitance) at the capacitive interface [60], suggesting that the morphology and arrangement of the obtained nanocarbons play important roles in determining the change of interfacial charge transfer resistance. For example, the clusters of engineered nanocarbons formed from the extended milling have more amorphous carbons with collapsed and compressed porous structures and thus diminish the charge transfer into deep sites of carbon clusters. Moreover, the Warburg regions are invisible for the pouch cells made with the graphite milled from 9 to 72 hrs, indicating the existence of short electrolyte ion diffusion paths in the electrode. The inset of **Fig. 5c** reveals the frequency responses of the ball-milled graphite tested in the pouch cells. the faster frequency response at the phase of -45° leads to a better rate capability. By increasing the milling time, the practical response frequency drops from 73.00 Hz (pristine graphite) to 8.62 Hz (BM200-18), then raise to 9.52 Hz (BM200-72), implying the rate capability retrieved a bit by the formation of engineered nanocarbons from the extended milling.

Fig. 5d shows gravimetric and volumetric energy densities of the pouch cells measured at a current density of 0.5 A g^{-1} . It is seen that both gravimetric and volumetric energy densities are firstly enhanced and then reduced with increasing the milling time. The BM200-18 exhibits the highest gravimetric energy density of 29.26 Wh kg^{-1} whereas the BM200-54 presents the highest volumetric energy density of 22.73 Wh L^{-1} at a current density of 0.5 A g^{-1} . **Fig. S10** shows the CV and GCD curves for the pouch cells of BM200-18 and BM200-54 at various scan rates and current densities, respectively. All CV curves retain the reasonable rectangular-like shape even at a high scan rate of 200 mV s^{-1} due to their good rate capabilities (**Fig. S10a, c**), and all GCD curves preserve the approximately symmetrical triangular owing to their good capacitive behaviors (**Fig. S10b, d**). The rate capabilities of these pouch cells in terms of gravimetric capacitance are shown in **Fig. S11** and the corresponding capacitance retentions calculated at the current density of 0.5 to 20 A g^{-1} are plotted in **Fig. 7d**. With increasing the milling time, the capacitance retention at 20 A g^{-1} firstly decreases from 49% (BM200-3) to 33% (BM200-36), then increases to 47% (BM200-72), which are consistent with the ESR and frequency response analysis. This is a general phenomenon for electrode materials with higher resistance or slower frequency response that results in a poorer rate capability. Compared to the pouch cells made with the commercial activated carbon (YP-50F) at a current density of 0.5 A g^{-1} , all pouch cells of the ball-milled graphite exhibit lower specific capacitance (maximum 69 F g^{-1} for BM200-18) than that of YP-50F (122 F g^{-1}). However, as shown in **Fig. 5e, f**, the areal and volumetric capacitances of graphite milled from 36 to 72 hrs are considerably higher than that of YP-50F, where the BM200-54 pouch cell shows the highest specific areal capacitance of 0.091 F m^{-2} and the highest volumetric capacitance of 53 F cm^{-3} at 0.5 A g^{-1} . In contrast, the YP-50F pouch cell, which was fabricated with the identical process, only exhibits a specific areal capacitance of 0.074 F m^{-2} and volumetric capacitance of 43 F cm^{-3} with no obvious capacitance retention at a current density of 20 A g^{-1} because of its high

porosity and tortuosity. The high-resolution TEM images shown in **Fig. 6** further demonstrate the different morphologies of BM200-18 and BM200-54. The inserts schematically illustrate that the electrolyte ion diffusion pathways can be directly affected by the morphologies and arrangements of nanocarbons engineered from different milling durations (e.g., 18 hrs and 54 hrs). Based on the same electrode volume for BM200-18 and BM200-54, BM200-18 has more complicated and longer ion diffusion pathways which need a longer fully charge-discharge time. However, BM200-54 has shorter ion diffusion pathways and better ion-accessible surface area for clusters of nanocarbons, contributing to a better volumetric capacitive performance.

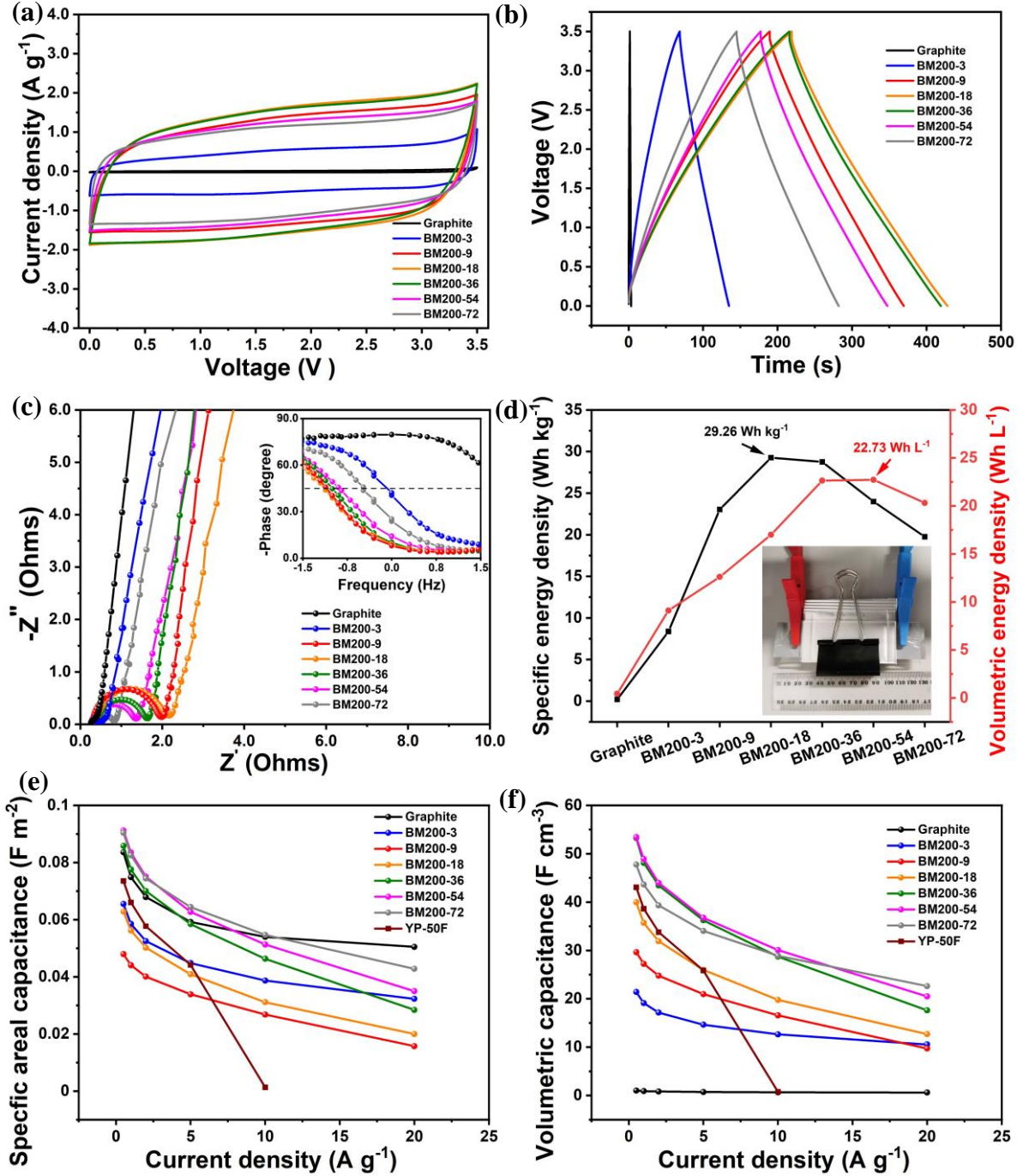


Fig. 5. Electrochemical testing results for pouch cells using neat EMIMBF₄ ionic liquid electrolyte. (a) CV curves tested at a scan rate of 50 mV s⁻¹. (b) GCD curves tested at a current density of 0.5 A g⁻¹. (c) Nyquist plots (the inset shows the Bode plots). (d) Evolution of energy densities at 0.5 A g⁻¹ (the inset shows the pouch cell for the test). (e) Specific areal capacitances and (d) volumetric capacitances of pouch cells fabricated with ball-milled graphite and YP-50F at various current densities from 0.5 A g⁻¹ to 20 A g⁻¹.

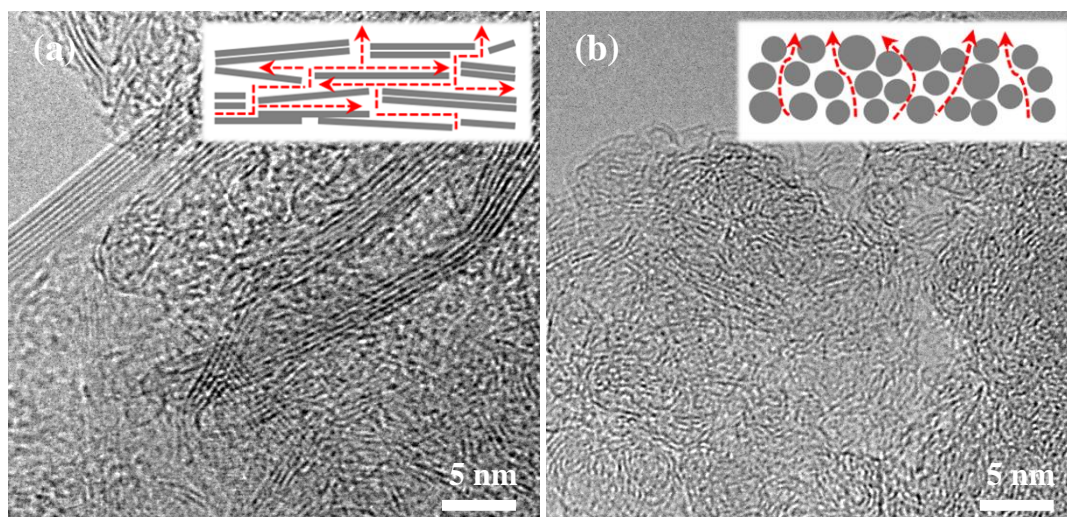


Fig. 6. High-resolution TEM images of (a) BM200-18 and (b) BM200-54 (the inset shows the ion diffusion pathways in the ball-milled graphite, BM200-54 has the shorter ion diffusion pathways and better ion accessible surface area compared to BM200-18).

Fig. 7a shows the R_{ct} and ESR of the YP-50F pouch cell from the Nyquist plot are much larger than those of the pouch cells made with the ball-milled graphite, confirming the poor rate performance of YP-50F in ionic liquid. After 11000 charge-discharge cycles at a high current density of 5 A g^{-1} , except for the pristine graphite, all charge transfer resistances of the pouch cells are significantly increased, which can result in the capacitance fading. However, all pouch cells made with the ball-milled graphite still demonstrate comparable long-term cycle stability with that of the YP-50F (**Fig. 7b**). To investigate the effect of packing compactness of carbon electrodes, we fabricated coin-type supercapacitors with the same electrolyte and the same carbon electrodes that were pressed under 10 MPa before assembling, the capacitance retentions after 11000 cycles at 5 A g^{-1} are dramatically increased to 77% for BM200-3, 73% for BM200-9, 72% for BM200-18, BM200-36, BM200-54 and 67% for BM200-72 while only 64% for YP-50F (**Fig. 7c**). In addition, the advantage of the high rate performance of BM200-54 and BM200-72 is diminished because the higher packing compactness can be achieved with their smaller particles compared to those of larger graphene-like sheets. Even so, the rate

capabilities of the ball-milled graphite are significantly enhanced, remaining ~20% higher than that of the YP-50F (**Fig. 7d**). As shown in **Fig. 7e**, although the differences in the specific capacitance at 0.5 A g⁻¹ between the pouch and coin cells are limited, the inset in shows that the IR drop of the coin cell at 5 A g⁻¹ is much smaller than that of its counterpart in the pouch cell. We believe that the much higher packing compactness with low ESR of coin cells improves their cycle stabilities and rate capabilities due to their better electrical interconnection between carbon clusters. Hence, the performance of our ionic liquid pouch-type supercapacitors made with green aqueous binder and the ball-milled graphite, in particular for their cycle stabilities and rate capabilities, can be significantly improved by using the industrial calendar roll machine with a pressing function.

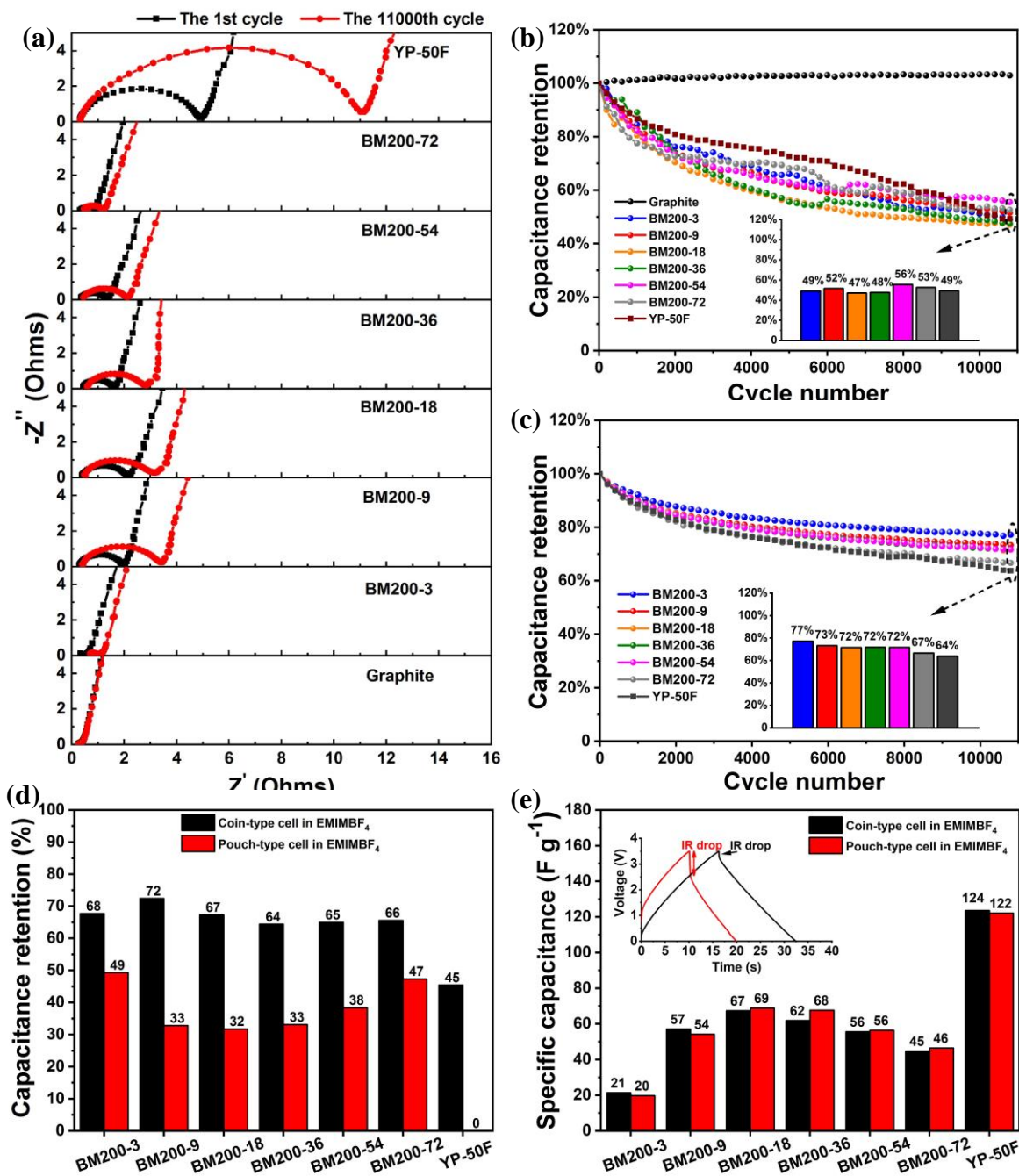


Fig. 7. Electrochemical testing results for pouch cells using neat EMIMBF₄ ionic liquid electrolyte. (a) Nyquist plots of pouch cells before and after cycle test. (b) and (c) Cycle stabilities of pouch cells and coin cells at 5 A g⁻¹, respectively (the inset shows capacitance retention after the cycle test). (d) Capacitance retention of pouch cells fabricated with the ball-milled graphite and YP-50F at current densities of 0.5 A g⁻¹ to 20 A g⁻¹. (e) Specific

capacitances of both pouch and coin cells at 0.5 A g⁻¹ (the inset shows GCD curves of both pouch and coin cells of BM200-18 at 5 A g⁻¹).

The Ragone plot was further used to evaluate the overall performance of the pouch cells fabricated with the ball-milled graphite. As shown in **Fig. 8a**, the BM200-18 pouch cell provides the highest gravimetric energy density of 29.26 Wh kg⁻¹ at a power density of 503.59 W kg⁻¹, which is smaller than 51.93 Wh kg⁻¹ at 477.07 W kg⁻¹ for YP-50F pouch cell. However, the BM200-18 pouch cell can still deliver 14.48 Wh kg⁻¹ at 21718.23 W kg⁻¹ while the YP-50F pouch cell only holds 0.93 Wh kg⁻¹ at 33427.19 W kg⁻¹, suggesting that BM200-18 exhibits a better rate performance with a lower gravimetric energy density compared with the YP-50F in ionic liquid electrolyte. However, as shown in **Fig. 8b**, the volumetric energy densities of the pouch cells for BM200-36, BM200-54 and BM200-72 are all higher than that of YP-50F. Among these, the BM200-54 pouch cell provides a remarkable volumetric energy density of 22.73 Wh L⁻¹ at a power density of 481.25 W L⁻¹ and still holds 12.79 Wh L⁻¹ at an extremely high power density of 23020.85 W L⁻¹, which are better than 16.43 Wh L⁻¹ at 351.07 W L⁻¹ and only 0.33 Wh L⁻¹ at 11783.50 W L⁻¹ for YP-50F pouch cell, evidencing the possibility of both outstanding rate capability and excellent volumetric energy density of the pouch-type supercapacitors made with the green aqueous binder and ball-milled graphite.

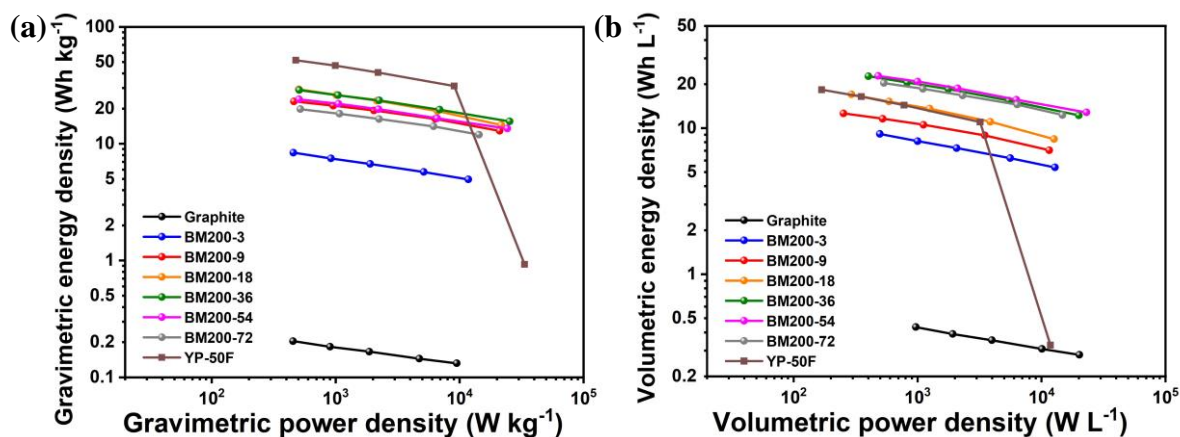


Fig. 8. (a) Gravimetric and (b) volumetric Ragone plots of pouch cells fabricated with ball-milled graphite and YP-50F.

4. Conclusion

Spherical nanocarbon clusters, acting as the electrode material of supercapacitors, can shorten the ion diffusion and facilitate ion accessibility, which result in better rate capability and volumetric energy density due to the effective interaction between the electrolyte ions and carbon electrodes. The spherical nanocarbon clusters produced by high-energy planetary ball-milling technique are in compact and disorder states with high contents of edge defects. Both micropores and mesopores are collapsed and compressed into a compact structure by prolonging the milling process, which increases the volumetric capacitance of carbon electrodes. We also demonstrated the feasibility of facile and sustainable production potential by fabricating pouch-type supercapacitors using neat EMIMBF₄ ionic liquid as the electrolyte, ball-milled graphite as electrode material, and CMC and SBR as the green aqueous binders. Both the outstanding rate capability and excellent volumetric energy density can be achieved for the pouch-type ionic liquid supercapacitors with the green aqueous binders and spherical nanocarbon clusters (i.e., extended milled graphite). Moreover, we proved that the performance

of pouch-type supercapacitors, in particular for their cycle stabilities and rate capabilities, will be significantly improved by using the industrial calendar roll machine with a pressing function.

Conflicts of interest

The authors declare no conflict of interest.

Acknowledgement

The authors would like to thank the financial support from the Australian Research Council Discovery Program of DP190103661 and DP220103229 and the Australian Government Research Training Program Scholarship.

References

- [1] Z. Zhao, K. Xia, Y. Hou, Q. Zhang, Z. Ye, J. Lu, Designing flexible, smart and self-sustainable supercapacitors for portable/wearable electronics: from conductive polymers, *Chem. Soc. Rev.*, 50 (2021) 12702-12743.
- [2] Y. Zhu, J. Deng, O. Fontaine, Breaking the strength barrier, *Nat. Energy*, 8 (2023) 643-644.
- [3] G. Pacchioni, Sustainable flexible supercapacitors, *Nat. Rev. Mater.*, 7 (2022) 844-844.
- [4] B.E. Conway, *Electrochemical supercapacitors: scientific fundamentals and technological applications*, Springer US, 1999.
- [5] S. Yasami, S. Mazinani, M. Abdouss, Developed composites materials for flexible supercapacitors electrode: “Recent progress & future aspects”, *J. Energy Storage*, 72 (2023) 108807.
- [6] S. Samantaray, D. Mohanty, I.M. Hung, M. Moniruzzaman, S.K. Satpathy, Unleashing recent electrolyte materials for next-generation supercapacitor applications: A comprehensive review, *J. Energy Storage*, 72 (2023) 108352.

- [7] A.G. Pandolfo, A.F. Hollenkamp, Carbon properties and their role in supercapacitors, *J. Power Sources*, 157 (2006) 11-27.
- [8] J. Ye, P. Simon, Y. Zhu, Designing ionic channels in novel carbons for electrochemical energy storage, *Natl. Sci. Rev.*, 7 (2019) 191-201.
- [9] Q. Wang, J. Yan, Z. Fan, Carbon materials for high volumetric performance supercapacitors: design, progress, challenges and opportunities, *Energy Environ. Sci.*, 9 (2016) 729-762.
- [10] Z. Zhang, S. Deng, D. Wang, Y. Qing, G. Yan, L. Li, Y. Wu, Low-tortuosity carbon electrode derived from Wood@ZIF-67 for supercapacitor applications, *Chem. Eng. J.*, 454 (2023) 140410.
- [11] F. Wang, J. Lee, L. Chen, G. Zhang, S. He, J. Han, J. Ahn, J.Y. Cheong, S. Jiang, I.-D. Kim, Inspired by Wood: Thick Electrodes for Supercapacitors, *ACS Nano*, 17 (2023) 8866-8898.
- [12] S. Li, Z. Li, D. Xu, G. Feng, R. Hu, Porosity and tortuosity: Keys for accurate modeling of porous electrodes in supercapacitors, *Mater. Today Phys.*, 36 (2023) 101174.
- [13] W. Zhang, W. Li, S. Li, Self-template activated carbons for aqueous supercapacitors, *Sustain. Mater. and Technol.*, 36 (2023) e00582.
- [14] C. Zhang, W. Lv, Y. Tao, Q.-H. Yang, Towards superior volumetric performance: design and preparation of novel carbon materials for energy storage, *Energy Environ. Sci.*, 8 (2015) 1390-1403.
- [15] Y. Fan, F. Fu, D. Yang, W. Liu, Z. Li, X. Qiu, Balancing the gravimetric and volumetric capacitance of nitrogen-enriched lignin porous carbon for high performance supercapacitors, *J. Energy Storage*, 63 (2023) 106947.
- [16] M. Xu, Q. Yu, Z. Liu, J. Lv, S. Lian, B. Hu, L. Mai, L. Zhou, Tailoring porous carbon spheres for supercapacitors, *Nanoscale*, 10 (2018) 21604-21616.

- [17] Y. Xiao, X. Cai, W. Sun, F. Yang, Nitrogen-enriched activated carbons via dual N-doping processes: Electrode material for high gravimetric- and volumetric-performance supercapacitor, *J. Energy Storage*, 56 (2022) 106040.
- [18] S. Feng, Z. Liu, Q. Yu, Z. Zhuang, Q. Chen, S. Fu, L. Zhou, L. Mai, Monodisperse Carbon Sphere-Constructed Pomegranate-Like Structures for High-Volumetric-Capacitance Supercapacitors, *ACS Appl. Mater. Interfaces*, 11 (2019) 4011-4016.
- [19] L. Yan, D. Li, T. Yan, G. Chen, L. Shi, Z. An, D. Zhang, N,P,S-Codoped Hierarchically Porous Carbon Spheres with Well-Balanced Gravimetric/Volumetric Capacitance for Supercapacitors, *ACS Sustain. Chem. Eng.*, 6 (2018) 5265-5272.
- [20] J. Dai, X. Wang, L. Xia, L. Luo, D. Li, C. Yang, Y. Xu, L. Dai, Template-free strategy for constructing polyaniline/polypyrrole derived carbon sphere as supercapacitors electrode use in acidic and alkaline electrolytes, *J. Energy Storage*, 55 (2022) 105436.
- [21] W. Zhang, W. Li, S. Li, Molten salt assisted self-activated carbon with controllable architecture for aqueous supercapacitor, *J. Mater. Sci. & Technol.*, 156 (2023) 107-117.
- [22] Y. Dong, S. Zhang, X. Du, S. Hong, S. Zhao, Y. Chen, X. Chen, H. Song, Boosting the Electrical Double-Layer Capacitance of Graphene by Self-Doped Defects through Ball-Milling, *Adv. Funct. Mater.*, 29 (2019) 1901127.
- [23] J. Feng, Y. Wang, Y. Xu, Y. Sun, Y. Tang, X. Yan, Ion regulation of ionic liquid electrolytes for supercapacitors, *Energy Environ. Sci.*, 14 (2021) 2859-2882.
- [24] H. Liu, H. Yu, Ionic liquids for electrochemical energy storage devices applications, *J. Mater. Sci. Technol.*, 35 (2019) 674-686.
- [25] T.S. Bhat, P.S. Patil, R.B. Rakhi, Recent trends in electrolytes for supercapacitors, *J. Energy Storage*, 50 (2022) 104222.
- [26] L. Sun, K. Zhuo, Y. Chen, Q. Du, S. Zhang, J. Wang, Ionic Liquid-Based Redox Active Electrolytes for Supercapacitors, *Adv. Funct. Mater.*, 32 (2022) 2203611.

- [27] C. Meng, F. Zhou, H. Liu, Y. Zhu, Q. Fu, Z.-S. Wu, Water-in-Salt Ambipolar Redox Electrolyte Extraordinarily Boosting High Pseudocapacitive Performance of Micro-supercapacitors, *ACS Energy Lett.*, 7 (2022) 1706-1711.
- [28] L. Yu, G.Z. Chen, Ionic Liquid-Based Electrolytes for Supercapacitor and Supercapattery, *Front. Chem.*, 7 (2019).
- [29] M. Armand, F. Endres, D.R. MacFarlane, H. Ohno, B. Scrosati, Ionic-liquid materials for the electrochemical challenges of the future, *Nat. Mater.*, 8 (2009) 621-629.
- [30] X. Liu, M.M. Vadiyar, J.K. Oh, Z. Ye, Designing Ultrasmall Carbon Nanospheres with Tailored Sizes and Textural Properties for High-Rate High-Energy Supercapacitors, *ACS Appl. Mater. Interfaces*, 13 (2021) 32916-32929.
- [31] Y. Chen, Y. Jiang, Z. Liu, L. Yang, Q. Du, K. Zhuo, Hierarchical porous N-doped graphene aerogel with good wettability for high-performance ionic liquid-based supercapacitors, *Electrochim. Acta*, 366 (2021) 137414.
- [32] M. Thommes, K. Kaneko, V. Neimark Alexander, P. Olivier James, F. Rodriguez-Reinoso, J. Rouquerol, S.W. Sing Kenneth, Physisorption of gases, with special reference to the evaluation of surface area and pore size distribution (IUPAC Technical Report), in: *Pure and Applied Chemistry*, 2015, pp. 1051.
- [33] T.S. Ong, H. Yang, Effect of atmosphere on the mechanical milling of natural graphite, *Carbon*, 38 (2000) 2077-2085.
- [34] Y. Zhu, S. Murali, M.D. Stoller, K.J. Ganesh, W. Cai, P.J. Ferreira, A. Pirkle, R.M. Wallace, K.A. Cychosz, M. Thommes, D. Su, E.A. Stach, R.S. Ruoff, Carbon-based supercapacitors produced by activation of graphene, *Science*, 332 (2011) 1537-1541.
- [35] M. Buzaglo, I.P. Bar, M. Varenik, L. Shunak, S. Pevzner, O. Regev, Graphite-to-Graphene: Total Conversion, *Adv. Mater.*, 29 (2017) 1603528.

- [36] M. Shtein, I. Pri-Bar, M. Varenik, O. Regev, Characterization of Graphene-Nanoplatelets Structure via Thermogravimetry, *Anal. Chem.*, 87 (2015) 4076-4080.
- [37] A. Sadezky, H. Muckenhuber, H. Grothe, R. Niessner, U. Pöschl, Raman microspectroscopy of soot and related carbonaceous materials: Spectral analysis and structural information, *Carbon*, 43 (2005) 1731-1742.
- [38] F. Barzegar, A. Bello, D. Momodu, M.J. Madito, J. Dangbegnon, N. Manyala, Preparation and characterization of porous carbon from expanded graphite for high energy density supercapacitor in aqueous electrolyte, *J. Power Sources*, 309 (2016) 245-253.
- [39] A.C. Ferrari, J. Robertson, Interpretation of Raman spectra of disordered and amorphous carbon, *Phys. Rev. B*, 61 (2000) 14095-14107.
- [40] P. Venezuela, M. Lazzeri, F. Mauri, Theory of double-resonant Raman spectra in graphene: Intensity and line shape of defect-induced and two-phonon bands, *Phys. Rev. B*, 84 (2011) 035433.
- [41] A. Cuesta, P. Dhamelincourt, J. Laureyns, A. Martínez-Alonso, J.M.D. Tascón, Raman microprobe studies on carbon materials, *Carbon*, 32 (1994) 1523-1532.
- [42] B. Dippel, H. Jander, J. Heintzenberg, NIR FT Raman spectroscopic study of flame soot, *Phys. Chem. Chem. Phys.*, 1 (1999) 4707-4712.
- [43] A. Eckmann, A. Felten, A. Mishchenko, L. Britnell, R. Krupke, K.S. Novoselov, C. Casiraghi, Probing the Nature of Defects in Graphene by Raman Spectroscopy, *Nano Lett.*, 12 (2012) 3925-3930.
- [44] J. Li, W. Zhang, X. Zhang, L. Huo, J. Liang, L. Wu, Y. Liu, J. Gao, H. Pang, H. Xue, Copolymer derived micro/meso-porous carbon nanofibers with vacancy-type defects for high-performance supercapacitors, *J. Mater. Chem. A*, 8 (2020) 2463-2471.

- [45] P. Dash, T. Dash, T.K. Rout, A.K. Sahu, S.K. Biswal, B.K. Mishra, Preparation of graphene oxide by dry planetary ball milling process from natural graphite, *RSC Adv.*, 6 (2016) 12657-12668.
- [46] T. Lin, I.W. Chen, F. Liu, C. Yang, H. Bi, F. Xu, F. Huang, Nitrogen-doped mesoporous carbon of extraordinary capacitance for electrochemical energy storage, *Science*, 350 (2015) 1508.
- [47] A.E.D. Mahmoud, A. Stolle, M. Stelter, Sustainable Synthesis of High-Surface-Area Graphite Oxide via Dry Ball Milling, *ACS Sustain. Chem. Eng.*, 6 (2018) 6358-6369.
- [48] I.-Y. Jeon, H.-J. Choi, M.J. Ju, I.T. Choi, K. Lim, J. Ko, H.K. Kim, J.C. Kim, J.-J. Lee, D. Shin, S.-M. Jung, J.-M. Seo, M.-J. Kim, N. Park, L. Dai, J.-B. Baek, Direct nitrogen fixation at the edges of graphene nanoplatelets as efficient electrocatalysts for energy conversion, *Sci. Rep.*, 3 (2013) 2260.
- [49] S. Rasul, A. Alazmi, K. Jaouen, M.N. Hedhili, P.M.F.J. Costa, Rational design of reduced graphene oxide for superior performance of supercapacitor electrodes, *Carbon*, 111 (2017) 774-781.
- [50] J. Gao, Y. Wang, H. Wu, X. Liu, L. Wang, Q. Yu, A. Li, H. Wang, C. Song, Z. Gao, M. Peng, M. Zhang, N. Ma, J. Wang, W. Zhou, G. Wang, Z. Yin, D. Ma, Construction of a sp^3/sp^2 Carbon Interface in 3D N-Doped Nanocarbons for the Oxygen Reduction Reaction, *Angew. Chem. Int. Ed.*, 58 (2019) 15089-15097.
- [51] D. Bhattacharjya, I.-Y. Jeon, H.-Y. Park, T. Panja, J.-B. Baek, J.-S. Yu, Graphene Nanoplatelets with Selectively Functionalized Edges as Electrode Material for Electrochemical Energy Storage, *Langmuir*, 31 (2015) 5676-5683.
- [52] Y. Wang, C. Li, H. Meng, Y. Lu, H. Fan, Production of functionalized graphitic carbon materials via solvent-free mechanochemical method for supercapacitors and water treatment, *Diam. Relat. Mater.*, 127 (2022) 109193.

- [53] S.R. Sivakkumar, A.S. Milev, A.G. Pandolfo, Effect of ball-milling on the rate and cycle-life performance of graphite as negative electrodes in lithium-ion capacitors, *Electrochim. Acta*, 56 (2011) 9700-9706.
- [54] I.-Y. Jeon, H.-J. Choi, S.-M. Jung, J.-M. Seo, M.-J. Kim, L. Dai, J.-B. Baek, Large-Scale Production of Edge-Selectively Functionalized Graphene Nanoplatelets via Ball Milling and Their Use as Metal-Free Electrocatalysts for Oxygen Reduction Reaction, *J. Am. Chem. Soc.*, 135 (2013) 1386-1393.
- [55] H.-Q. Li, Y.-G. Wang, C.-X. Wang, Y.-Y. Xia, A competitive candidate material for aqueous supercapacitors: High surface-area graphite, *J. Power Sources*, 185 (2008) 1557-1562.
- [56] N.C. Deb Nath, I.-Y. Jeon, M.J. Ju, S.A. Ansari, J.-B. Baek, J.-J. Lee, Edge-carboxylated graphene nanoplatelets as efficient electrode materials for electrochemical supercapacitors, *Carbon*, 142 (2019) 89-98.
- [57] F. Yang, Y. Cao, Z. Chen, X. He, L. Hou, Y. Li, Large-scale preparation of B/N co-doped graphene-like carbon as an efficient metal-free catalyst for the reduction of nitroarenes, *New J. Chem.*, 42 (2018) 2718-2725.
- [58] E. Gomibuchi, T. Ichikawa, K. Kimura, S. Isobe, K. Nabeta, H. Fujii, Electrode properties of a double layer capacitor of nano-structured graphite produced by ball milling under a hydrogen atmosphere, *Carbon*, 44 (2006) 983-988.
- [59] J. Hong, S. Fan, Y. Wu, C. Wang, Z. Li, J. Chen, S. Zhong, Xylitol-assisted ball milling of graphite to prepare long-cycle and high-capacity graphene nanosheet as lithium-ion anode materials, *J. Mater. Sci.*, 56 (2021) 18200-18209.
- [60] J.K. Ewert, D. Weingarth, C. Denner, M. Friedrich, M. Zeiger, A. Schreiber, N. Jäckel, V. Presser, R. Kempe, Enhanced capacitance of nitrogen-doped hierarchically porous carbide-derived carbon in matched ionic liquids, *J. Mater. Chem. A*, 3 (2015) 18906-18912.

- High-density spherical nanocarbon clusters are produced by mass-production method.
- The spherical morphology, close arrangement and high density shorten the ion transport pathway.
- The collapsed micropores and mesopores increase the volumetric capacitance.
- The ionic liquid pouch-type supercapacitors show superior volumetric performance.

Declaration of interests

☒The authors declare that they have no known competing financial interests or personal relationships that could have appeared to influence the work reported in this paper.

☐The authors declare the following financial interests/personal relationships which may be considered as potential competing interests:



27 September 2023

Editor
Journal of Energy Storage

Dear Editor,

We are writing to submit our manuscript entitled **“High-Density Spherical Nanocarbon Clusters for Eco-Friendly Pouch-Type Ionic Liquid Supercapacitors with High Volumetric Energy Density and Rate Performance”** for your consideration of publishing in Journal of Energy Storage. The material contained in this paper is original and is not under consideration for publication elsewhere.

Novelty and significance of this work:

Here, we developed a scalable and sustainable approach to produce high-density spherical nanocarbon clusters as the electrode material of pouch-type ionic liquid supercapacitors. What we found and did in this work is shown below:

1. The obtained spherical morphologies, close arrangements and high densities of nanocarbon clusters can shorten the ion transport pathway and facilitate ion accessibility for better capability and volumetric energy density.
2. The collapsed micropores and mesopores resulted from extended high-energy milling increase the compact density, thus increase the volumetric capacitance.
3. We demonstrated the feasibility of facile and sustainable production potential by fabricating pouch-type supercapacitors using neat EMIMBF₄ ionic liquid as the electrolyte, ball-milled graphite as electrode material, and CMC and SBR as the green aqueous binders. The fabricated supercapacitor exhibits superior volumetric energy density and rate capability compared with the commercial activated carbons (YP-50F).
4. The performance of supercapacitors, in particular for their cycle stabilities and rate capabilities can be significantly improved by using the industrial calendar roll machine with a pressing function.

We envisage that our latest and comprehensive experimental results based on high-density spherical nanocarbon clusters will not only become an encyclopaedic referencing source for industrial supercapacitors in their specificity, but also provide the relevant research community with a pragmatic example of exploring new perspective with the existing engineering technique to enable sustainably and cost-effectively manufacturing the high-performance supercapacitors in high throughput production. We believe that such a goal is highly aligned with that of Journal of Energy Storage, thus it is the best vehicle to deliver our work.

If you need any further information or clarification on this matter, please let me know. Thank you very much for your consideration.

Journals (related to capacitive materials/supercapacitors) published by the team:

Sustainable Materials and Technologies 36, e00582, 2023

Journal of Materials Science & Technology 156, 107-117, 2023

Nature 605 (7909), 262-267, 2022

Journal of Energy Chemistry 71, 234-265, 2022

Yours sincerely

A handwritten signature in black ink, appearing to read '李文献' (Li Wenxian).

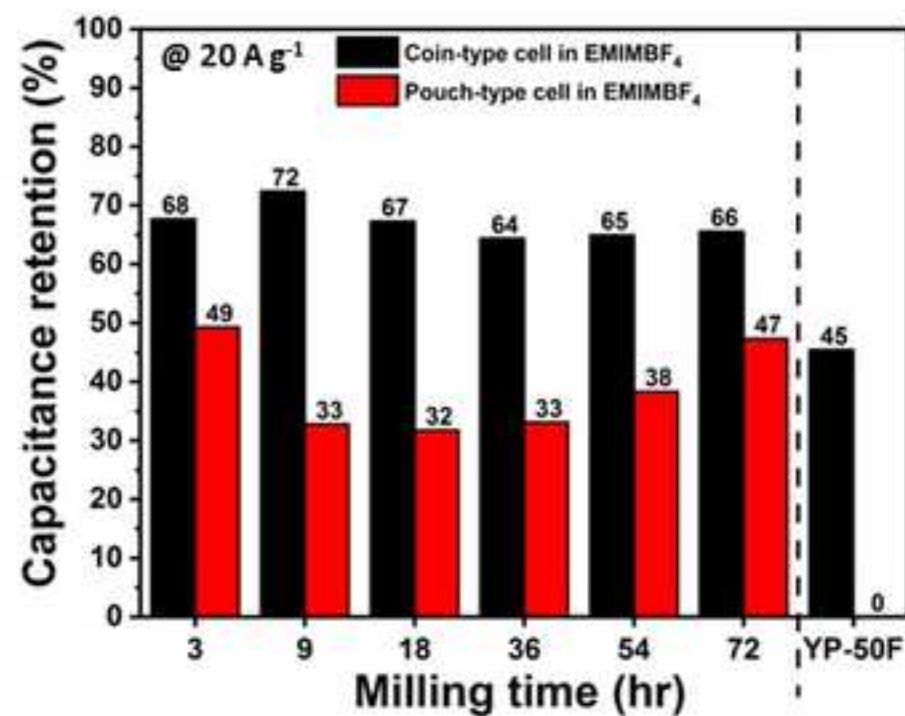
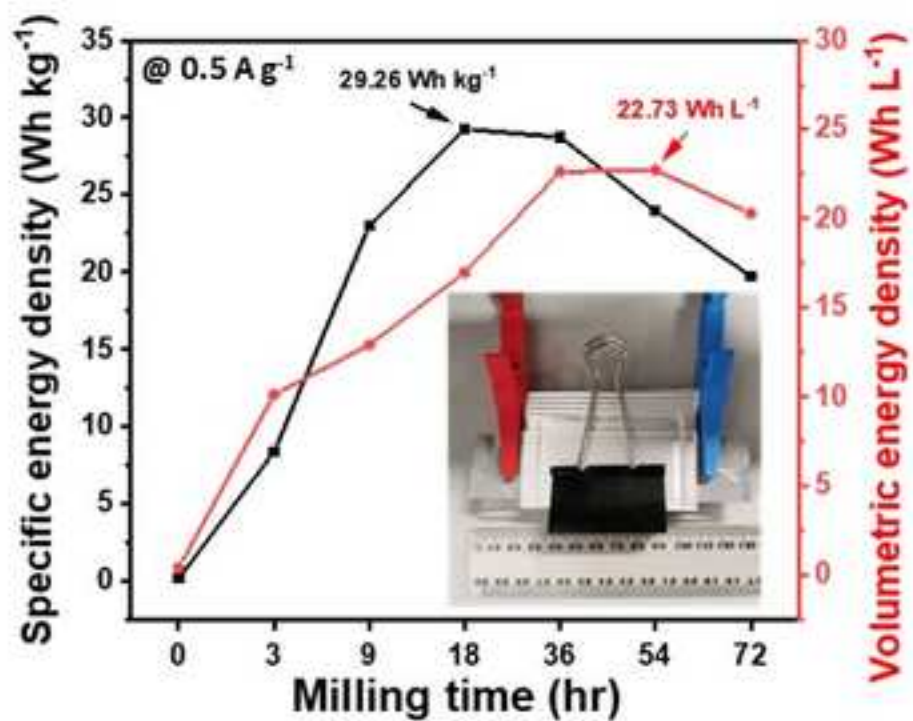
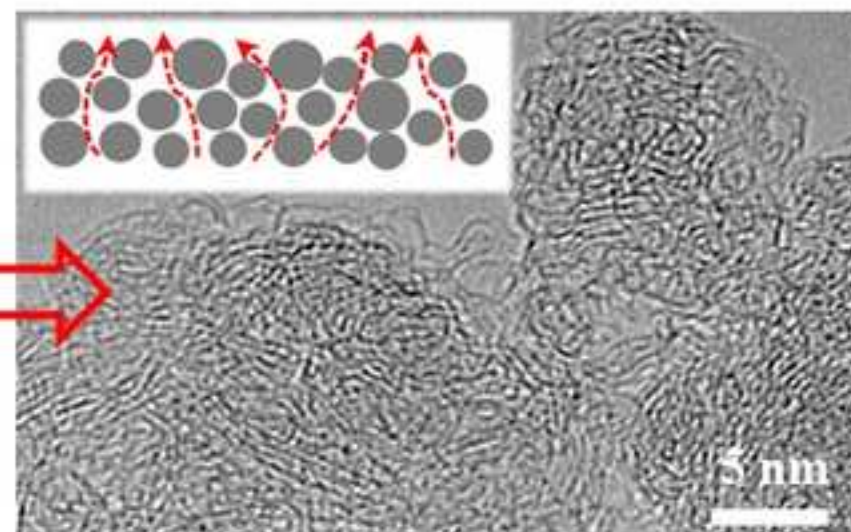
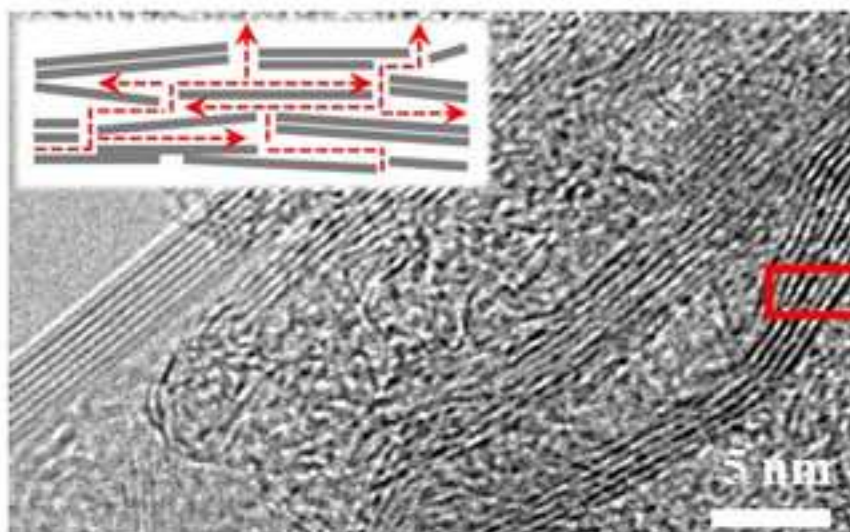
Wenxian Li, Ph.D

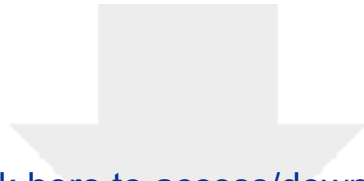
Senior Research Associate, School of Materials Science and Engineering

UNSW Materials and Manufacturing Futures Institute

The University of New South Wales

Sydney 2052 Australia





[Click here to access/download](#)

Supplementary Material

BM_Supporting Information_JES.docx

